Monthly Notices
of the
ROYAL ASTRONOMICAL SOCIETY

Mon. Not. R. Astron. Soc. **408,** 1658–1665 (2010) doi:10.1111/j.1365-2966.2010.17228.x

BOOMERanG constraints on primordial non-Gaussianity from analytical Minkowski functionals

P. Natoli,[1,2⋆] G. De Troia,[1] C. Hikage,[3,4] E. Komatsu,[5] M. Migliaccio,[1] P. A. R. Ade,[4] J. J. Bock,[6] J. R. Bond,[7] J. Borrill,[8,9] A. Boscaleri,[10] C. R. Contaldi,[11] B. P. Crill,[6] P. de Bernardis,[12] G. de Gasperis,[1] A. de Oliveira-Costa,[13] G. Di Stefano,[14] E. Hivon,[15] T. S. Kisner,[8,9] W. C. Jones,[16] A. E. Lange,[17] S. Masi,[12] P. D. Mauskopf,[4] C. J. MacTavish,[18] A. Melchiorri,[12,19] T. E. Montroy,[20] C. B. Netterfield,[21] E. Pascale,[21] F. Piacentini,[12] G. Polenta,[12,22,23] S. Ricciardi,[8,9] G. Romeo,[14] J. E. Ruhl,[20] M. Tegmark,[13] M. Veneziani[12] and N. Vittorio[1]

[1]*Dipartimento di Fisica, Università di Roma 'Tor Vergata', Via della Ricerca Scientifica, 1 I-00133 Roma, Italy*
[2]*INFN, Sezione di Tor Vergata, Via della Ricerca Scientifica 1, I-00133 Roma, Italy*
[3]*Department of Astrophysical Sciences, Princeton University, Peyton Hall, Princeton, NJ 08544, USA*
[4]*School of Physics and Astronomy, Cardiff University, Cardiff CF24 3AA*
[5]*Texas Cosmology Center, University of Texas at Austin, 1 University Station, C1400, Austin, TX 78712, USA*
[6]*Jet Propulsion Laboratory, Pasadena, CA 91109-8099, USA*
[7]*Canadian Institute for Theoretical Astrophysics, University of Toronto, 60 St George Street, Toronto, Ontario M5S 3H8, Canada*
[8]*Computational Research Division, Lawrence Berkeley National Laboratory, Berkeley, CA 94720, USA*
[9]*Space Sciences Laboratory, UC Berkeley, CA 94720, USA*
[10]*IFAC-CNR, I-50127 Firenze, Italy*
[11]*Theoretical Physics Group, Imperial College, London SW7 2BZ*
[12]*Dipartimento di Fisica, Università La Sapienza, I-00185 Roma, Italy*
[13]*Department of Physics, MIT, Cambridge, MA 02139, USA*
[14]*Istituto Nazionale di Geofisica e Vulcanologia, 00143 Rome, Italy*
[15]*Institut d'Astrophysique, Paris 75014, France*
[16]*Department of Physics, Princeton University, Princeton, NJ 08544, USA*
[17]*Observational Cosmology, California Institute of Technology, Pasadena, CA 91125, USA*
[18]*Astrophysics Group, Imperial College, London SW7 2BZ*
[19]*INFN, Sezione di Roma 1, I-00185 Roma, Italy*
[20]*Physics Department, Case Western Reserve University, Cleveland, OH 44106, USA*
[21]*Physics Department, University of Toronto, Toronto, Ontario M5S 3H8, Canada*
[22]*ASI Science Data Center, c/o ESRIN, 00044 Frascati, Italy*
[23]*INAF – Osservatorio Astronomico di Roma, I-00040 Monte Porzio Catone, Italy*

Accepted 2010 June 21. Received 2010 May 18; in original form 2009 June 2

ABSTRACT

We use Minkowski functionals (MFs) to constrain a primordial non-Gaussian contribution to the cosmic microwave background intensity field as observed in the 150- and 145-GHz BOOMERanG maps from the 1998 and 2003 flights, respectively, performing for the first time a joint analysis of the two data sets. A perturbative expansion of the MF formulae in the limit of a weakly non-Gaussian field yields analytical formulae, derived by Hikage et al., which can be used to constrain the coupling parameter $f_{\rm NL}$ without the need for non-Gaussian simulations. We find $-770 < f_{\rm NL} < 500$ at 95 per cent CL, significantly improving the previous constraints by De Troia et al. on the BOOMERanG 2003 data set. These are the best $f_{\rm NL}$ limits to date for suborbital probes.

Key words: methods: analytical – methods: statistical – early Universe – cosmic background radiation – cosmology: observations.

1 INTRODUCTION

Detection of non-Gaussian signals in the cosmic microwave background (CMB) anisotropy pattern can be of significant help in

⋆E-mail: paolo.natoli@gmail.com

discriminating between different inflationary models. The simplest inflationary models based on single-rolling scalar fields predict very small deviations from Gaussianity that cannot be usefully constrained by present-day experimental efforts (Bartolo et al. 2004). However, multifield inflationary models and other alternative scenarios allow for more relevant non-Gaussian contribution that could be in principle detected by current and forthcoming missions (Bernardeau & Uzan 2002; Lyth, Ungarelli & Wands 2003). In this paper we consider only the so-called local form for primordial non-Gaussianity, which can be parametrized by means of a quadratic term in Bardeen's curvature perturbations Φ (Salopek & Bond 1990; Gangui et al. 1994; Verde et al. 2000; Komatsu & Spergel 2001):

$$\Phi(\boldsymbol{x}) = \Phi_G(\boldsymbol{x}) + f_{\rm NL}\left[\Phi_G(\boldsymbol{x})^2 - \left\langle \Phi_G(\boldsymbol{x})^2 \right\rangle\right], \quad (1)$$

where Φ_G is a zero mean, Gaussian random field and $f_{\rm NL}$ is the coupling parameter that characterizes the amplitude of primordial non-Gaussianity. At present, the most stringent limits on $f_{\rm NL}$ are derived from the *Wilkinson Microwave Anisotropy Probe* (*WMAP*) 5-yr analysis at $-4 < f_{\rm NL} < 80$ (95 per cent CL) using an optimal (i.e. minimum variance) bispectrum based estimator (Smith, Senatore & Zaldarriaga 2009); the recently published *WMAP* 7-yr analysis (Komatsu et al. 2010) has yielded a comparable $-10 < f_{\rm NL} < 74$ (again, 95 per cent CL). Many teams have further analysed the *WMAP* data set to yield constraints on $f_{\rm NL}$ using a plethora of tests, including wavelet-based estimators: see e.g. Curto, Martínez-González & Barreiro (2009), Rudjord et al. (2010), Pietrobon et al. (2009), and references therein. All $f_{\rm NL}$ limits to date are compatible with a Gaussian hypothesis. Yadav & Wandelt (2008) claimed a measure of a positive $f_{\rm NL}$ at above 99.5 per cent CL in the *WMAP* 3-yr data using a bispectrum-based statistics; however, their claimed signal has not been confirmed by the *WMAP* 5- and 7-yr analyses (Komatsu et al. 2009; Smith et al. 2009; Komatsu et al. 2010).

On the other hand, several groups have also investigated specific signatures in the *WMAP* data, typically induced by low-resolution features such as anomalous spots, reporting high significance yet unmodelled detection of non-Gaussianity (Vielva et al. 2004; Creminelli et al. 2007; Cruz et al. 2007; Eriksen et al. 2007; Park, Park & Gott 2007; Räth et al. 2009).

CMB suborbital experiments have also delivered $f_{\rm NL}$ constraints, particularly MAXIMA (Santos et al. 2003), VSA (Smith et al. 2004), BOOMERanG (De Troia et al. 2007) and ARCHEOPS (Curto et al. 2008). Although such limits are weaker than those based on *WMAP*, they probe a range of angular scale that will not be accessible to space-borne observation until the advent of *Planck*.[1] Among suborbital probes, De Troia et al. (2007) set the most stringent $f_{\rm NL}$ constraints to date at $-800 < f_{\rm NL} < 1050$ (95 per cent CL) from BOOMERanG 2003 (hereafter B03) data set using a pixel-space statistics based on Minkowski functionals (MFs). Such constraints were obtained using a reference Monte Carlo set composed of non-Gaussian CMB maps.

In this paper we revisit the $f_{\rm NL}$ analysis of the BOOMERanG data set. We employ a larger data set that also includes the BOOMERanG 1998 (hereafter B98) data, allowing for a larger sky coverage and improved signal-to-noise ratio (S/N). Furthermore, we apply a different, harmonic based, MF code that overcomes a weakness of the previous B03 analysis, which used a flat-sky approximation to compute the functionals. Finally, we employ the perturbative approach developed by Hikage, Komatsu & Matsubara (2006) to quantify the contribution of primordial non-Gaussianity to MF. Hikage et al. (2008) successfully applied the perturbative method to *WMAP* data without the need of a large set of non-Gaussian simulations.

The plan of this paper is as follows. In Section 2 we briefly describe the BOOMERanG experiment and the two data sets it has produced as well as our data analysis pipeline. In Section 3 we apply the perturbative formulae to compute the MFs of the data and Gaussian Monte Carlo simulation maps. Furthermore in Section 4 we constrain $f_{\rm NL}$ and in Section 5 we draw our main conclusions.

2 THE B98 AND B03 DATA SETS

BOOMERanG was launched for the first time from Antarctica in 1998 December. It has observed the sky for about 10 d, centring a target region at RA $\sim 5^{\rm h}$ and Dec. $\sim -45^\circ$ that is free of contamination by thermal emission from interstellar dust. BOOMERanG mapped this region scanning the telescope through 60° at fixed elevation and at constant speed. At intervals of a few hours the telescope elevation was changed in order to increase the sky coverage (Crill et al. 2003). The survey region aimed at CMB observations is $\sim$3 per cent of the sky or $\sim$1200 deg^2 (Ruhl et al. 2003). The data were obtained using 16 spider-web bolometric detectors sensitive to four frequency bands centred at 90, 150, 240 and 410 GHz. Here we restrict ourselves to the 150-GHz data that have the most advantageous combination of sensitivity and angular resolution to target the CMB fluctuations. The analysis of B98 data set produced the first high-S/N CMB maps at subdegree resolution and one of the first high-confidence measurements of the first acoustic peak in the CMB anisotropy angular spectrum (de Bernardis et al. 2000). The Gaussianity of this data set has been constrained in both pixel and harmonic space (Polenta et al. 2002; De Troia et al. 2003).

The B03 experiment has been flown from Antarctica in 2003. Contrarily to B98, B03 was capable of measuring linear polarization other than total intensity (Jones et al. 2006; MacTavish et al. 2006; Montroy et al. 2006; Piacentini et al. 2006). It has observed the microwave sky for $\sim$7 d in three frequency bands, centred at 145, 245 and 345 GHz. Here we use only the 145-GHz data, for reasons analogous to B98. These have been gathered with polarization-sensitive bolometers (PSBs), i.e. bolometers sensitive to total intensity and a combination of the two Stokes linear polarization parameters Q and U (Jones et al. 2003). The analysis of the data set has produced high-quality maps (Masi et al. 2006) of the southern sky that have been conveniently divided in three regions: a 'deep' (in terms of integration time per pixel) survey region ($\sim$90 deg^2) and a 'shallow' survey region ($\sim$750 deg^2), both at high Galactic latitudes, as well as a region of $\sim$300 deg^2 across the Galactic plane. The deep region is completely embedded in the shallow region.

In this paper we apply a pixel mask to select a larger effective sky region than the one used in De Troia et al. (2007). We have been extremely careful in choosing this sky cut, rejecting regions potentially contaminated by foreground emission, which shows up clearly in the B98 higher frequency maps, and pixels falling too close to the edge of the survey region, which exhibit low S/N and potential visual artefacts. The final cut we use covers about 980 deg^2 or 2.4 per cent of the sky. This should be compared with the $\sim$700 (1.7 per cent of the sky) employed for De Troia et al. (2007), which only used B03, and with the 1.2 and 1.8 per cent of the sky selected, respectively, for the B98 analyses of Polenta et al. (2002) and De Troia et al. (2003). The useful sky fraction considered in this paper is the largest ever used for BOOMERanG non-Gaussianity studies.

We analysed the temperature (T) data map reduced jointly from eight PSBs at 145 GHz (Masi et al. 2006) for the B03 data set and the

[1] http://www.rssd.esa.int/index.php?project=planck

T map obtained from the best three of the six 150-GHz channels for B98. While we do not consider here the Stokes *Q* and *U* polarization maps, the B03 temperature map has been marginalized with respect to linear polarization. The maps have been produced with ROMA, an iterative generalized least-squares (GLS) map-making code specifically tuned for BOOMERanG analysis (Natoli et al. 2001; De Gasperis et al. 2005). To work, the GLS map maker needs to know the detectors' noise power spectral densities, which is estimated directly from flight data using an iterative procedure. In the case of B03, where cross-talks among PSBs located in the same feed horn are significant, we have also estimated the corresponding noise cross-spectra (Masi et al. 2006). The timelines have been carefully flagged to exclude unwanted data; for B98, only the more conservative part of the scan surveyed at 1 degree per second (dps) is used (Crill et al. 2003) while for both data sets we have flagged all of the turn-around data. Once the B98 and B03 maps are produced, we obtain a single data map by noise-weighting the two. In doing so we treat the residual noise left in the map as white. This choice is motivated by a property of the GLS map-making procedure, which is very effective in suppressing the level of noise correlations in the data. The noise level in the B98 map roughly equals that in the B03 shallow region: at 6.7 arcmin the noise rms is about 40 μK pixel^{-1}. (While the B98 flight actually lasted longer than B03, we consider only three channels and the 1 dps part of the scan here.) The noise rms in the B03 deep region is $\sim$10 μK for 6.7 arcmin pixels. The joint B03/B98 map we obtain is shown in Fig. 1 in the sky cut employed for the analysis hereafter.

To probe CMB non-Gaussianity it is important to keep under control contaminations from astrophysical foregrounds, whose pattern is markedly non-Gaussian. In the region selected here, foreground intensity is known to be negligible with respect to the cosmological signal (Masi et al. 2006). We have masked all detectable sources in the observed field. To assess the robustness of our tests of Gaussianity we used a set of 1000 Monte Carlo simulation maps that mimic both the B03 and the B98 data. To produce these simulations, the following scheme is employed. The Gaussian CMB sky signal is simulated using the cosmological parameters estimated from the *WMAP* 1-yr data (Hinshaw et al. 2003) which fits well the BOOMERanG temperature power spectrum. This signal is smoothed according to the measured optical beam and synthesized into a pixelized sky map, using HEALPIX routines (Górski et al. 2005). Taking into account the B03 and B98 scanning strategy, the signal map is projected on to eight timestreams, one for each 145-GHz detector, for B03 and on to three timestreams for the B98 150-GHz channels we consider here. Noise-only timestreams are also produced as Gaussian realizations of each detector's noise power spectral density, iteratively estimated from flight data as explained above, fully taking into account correlated noise and, in the case of B03, also cross-talks between detectors hosted within the same optical horn. The signal and noise timelines are then added together. To reduce the simulated timelines, we follow the same steps performed when analysing real data: the timelines are then reduced with the ROMA map-making code replicating the actual flight pointing and transient flagging to produce *T* maps jointly from three B98 channels and *T*, *Q* and *U* maps jointly from all eight B03 channels. We enforce that the map-making procedure is applied to simulation and observational data following the same steps.

It is worth noting that in this paper the B98 and B03 data have been used to produce a joint map for the first time.

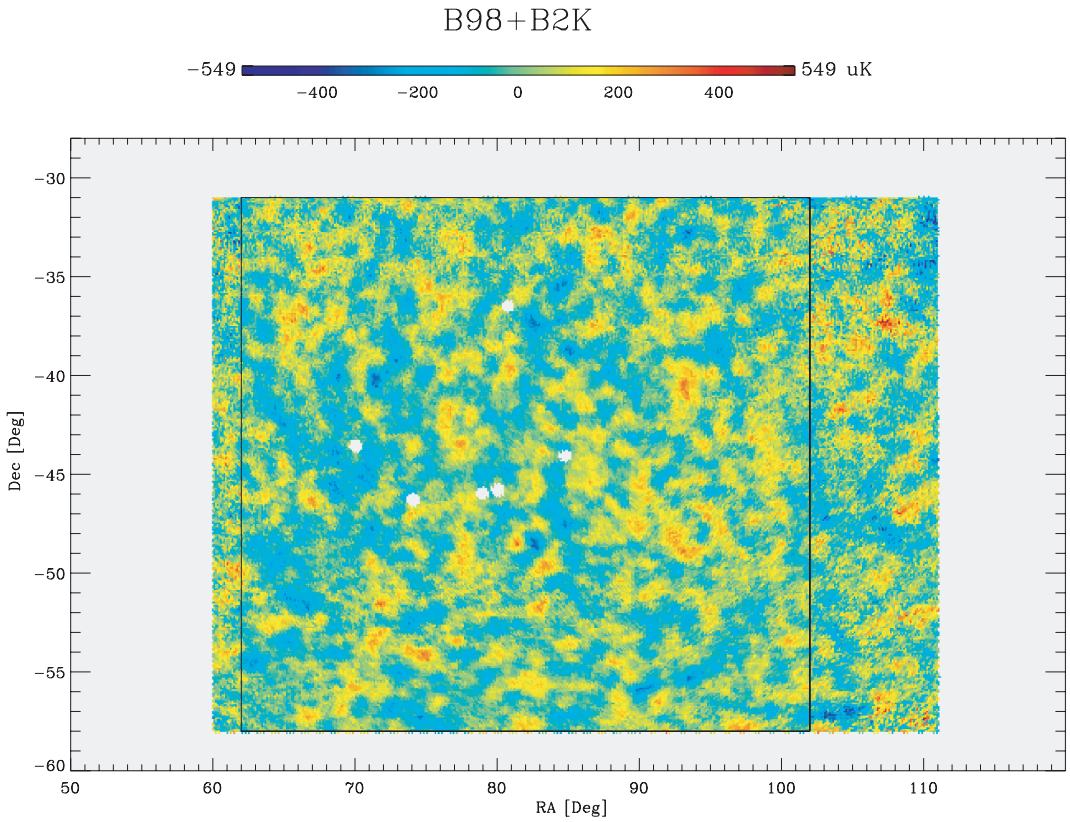

Figure 1. The CMB field as seen in the B2K + B98 map, in the sky cut used for the analysis presented here. The solid line shows the boundary of the region taken in consideration for the analysis in De Troia et al. (2007).

3 PERTURBATIVE APPROACH TO MINKOWSKI FUNCTIONAL FOR A WEAKLY NON-GAUSSIAN CMB FIELD

In the previous paper (De Troia et al. 2007) we have also applied simple pixel-based analysis (specifically, the normalized skewness and kurtosis) to the B03 observed field. Here we restrict ourselves to three MFs generally defined in two-dimensional maps: fraction of area V_0, total circumference V_1 and Euler characteristic V_2. We measure the MFs for CMB temperature maps above the threshold density ν, defined as the temperature fluctuation $f \equiv \Delta T/T$ normalized by its standard deviation $\sigma \equiv \langle f^2 \rangle^{1/2}$. Following the formalism by Matsubara (2003) and Hikage et al. (2006), we can write the analytical formula for the kth MF of weakly non-Gaussian fields as

$$V_k(\nu) = \frac{1}{(2\pi)^{(k+1)/2}} \frac{\omega_2}{\omega_{2-k}\omega_k} \left(\frac{\sigma_1}{\sqrt{2}\sigma_0}\right)^k \mathrm{e}^{-\nu^2/2} \times \left\{ H_{k-1}(\nu) + \left[\frac{1}{6} S^{(0)} H_{k+2}(\nu) + \frac{k}{3} S^{(1)} H_k(\nu) + \frac{k(k-1)}{6} S^{(2)} H_{k-2}(\nu) \right] \sigma_0 + O\left(\sigma_0^2\right) \right\}, \quad (2)$$

where $H_n(\nu)$ are the Hermite polynomials and $\omega_k = \pi^{k/2}\Gamma(k/2+1)$ gives $\omega_0 = 1$, $\omega_1 = 2$ and $\omega_2 = \pi$. The $S^{(i)} (i = 0, 1, 2)$ are skewness parameters, defined by

$$S^{(0)} \equiv \frac{\langle f^3 \rangle}{\sigma_0^4}, \quad (3)$$

$$S^{(1)} \equiv -\frac{3}{4} \frac{\langle f^2 (\nabla^2 f) \rangle}{\sigma_0^2 \sigma_1^2}, \quad (4)$$

$$S^{(2)} \equiv -3 \frac{\langle (\nabla f) \cdot (\nabla f)(\nabla^2 f) \rangle}{\sigma_1^4}. \quad (5)$$

The variances σ_j^2 ($j = 0, 1$) are calculated from C_ℓ as

$$\sigma_j^2 \equiv \frac{1}{4\pi} \sum_\ell (2\ell+1) \left[\ell(\ell+1)\right]^j C_\ell W_\ell^2, \quad (6)$$

where W_ℓ is a window function that includes the experiment's effective optical transfer function (assumed circularly symmetric) and low- and high-ℓ cut-off as well as the filter function due to pixelization effects. Expanding the skewness parameters into spherical harmonics and using the reduced bispectrum $b_{\ell_1\ell_2\ell_3}$ as a function of $f_{\rm NL}$ (Komatsu & Spergel 2001), we get

$$S^{(0)} = \frac{3}{2\pi\sigma_0^4} \sum_{2 \le \ell_1 \le \ell_2 \le \ell_3} I^2_{\ell_1\ell_2\ell_3} b_{\ell_1\ell_2\ell_3} W_{\ell_1} W_{\ell_2} W_{\ell_3}, \quad (7)$$

$$S^{(1)} = \frac{3}{8\pi\sigma_0^2\sigma_1^2} \sum_{2 \le \ell_1 \le \ell_2 \le \ell_3} [\ell_1(\ell_1+1) + \ell_2(\ell_2+1) + \ell_3(\ell_3+1)] I^2_{\ell_1\ell_2\ell_3} b_{\ell_1\ell_2\ell_3} W_{\ell_1} W_{\ell_2} W_{\ell_3}, \quad (8)$$

$$S^{(2)} = \frac{3}{4\pi\sigma_1^4} \sum_{2 \le \ell_1 \le \ell_2 \le \ell_3} \{[\ell_1(\ell_1+1) + \ell_2(\ell_2+1) - \ell_3(\ell_3+1)]\ell_3(\ell_3+1) + (\mathrm{cyc.})\} \times I^2_{\ell_1\ell_2\ell_3} b_{\ell_1\ell_2\ell_3} W_{\ell_1} W_{\ell_2} W_{\ell_3}, \quad (9)\text{–}(10)$$

where

$$I_{l_1 l_2 l_3} \equiv \sqrt{\frac{(2l_1+1)(2l_2+1)(2l_3+1)}{4\pi}} \begin{pmatrix} l_1 & l_2 & l_3 \\ 0 & 0 & 0 \end{pmatrix}. \quad (11)$$

In the above theoretical predictions we assume a ΛCDM model with the cosmological parameters at the maximum likelihood peak from *WMAP* 1-yr data (Spergel et al. 2003): $\Omega_{\rm b} = 0.043$, $\Omega_{\rm cdm} = 0.21$, $\Omega_\Lambda = 0.74$, $H_0 = 72\,{\rm km\,s^{-1}\,Mpc^{-1}}$, $n_{\rm s} = 0.96$ and $\tau = 0.11$. The amplitude of primordial fluctuations has been normalized to the first peak amplitude of the temperature power spectrum, $\ell(\ell+1)C_\ell/(2\pi) = (74.7\,\mu{\rm K})^2$ at $\ell = 220$ (Page et al. 2003).

We compute the MFs of the pixelized maps by integrating a combination of first and second angular derivatives of the temperature over the sky, as described in appendix A.1. of Hikage et al. (2006). The threshold density ν is set in the range -3.6 to 3.6, assuming 19 evenly spaced grid points. For our analysis we use maps at HEALPIX (Górski et al. 2005) resolution of ∼13 arcmin ($N_{\rm side} = 256$) and ∼7 arcmin ($N_{\rm nside} = 512$).

4 CONSTRAINTS ON PRIMORDIAL NON-GAUSSIANITY

We define a 'joint' estimator by grouping the V_k values in a single, 57-element data vector $V_J \equiv \{V_0(\nu = -3.6), V_0(\nu = -3.2), \ldots, V_0(\nu = 3.6), V_1(\nu = -3.6), \ldots, V_2(\nu = 3.6)\}$. We want now to constrain the $f_{\rm NL}$ parameter and estimate its best-fitting value. Starting from analytical formulae we can calculate the non-Gaussian part of the MFs using equation (2), i.e.

$$\Delta V_J(f_{\rm NL}) = V_J(f_{\rm NL}) - V_J(f_{\rm NL} = 0). \quad (12)$$

We can then estimate our final non-Gaussian predictions as

$$\tilde{V}_J(f_{\rm NL}) = \bar{V}_J(f_{\rm NL} = 0) + \Delta V_J(f_{\rm NL}), \quad (13)$$

where $\bar{V}_J(f_{\rm NL} = 0)$ is the average MF computed from our Gaussian Monte Carlo simulations. The reason for this choice is that the Monte Carlo average provides an accurate estimate of the MFs, accounting for instrumental and coverage effect. Finally we perform a χ^2 analysis by measuring

$$\chi^2 = \sum_{JJ'} \left[V_J^{\rm B98+B03} - \tilde{V}_J(f_{\rm NL})\right] C^{-1}_{J,J'} \left[V_{J'}^{\rm B98+B03} - \tilde{V}_{J'}(f_{\rm NL})\right], \quad (14)$$

where $V_J^{\rm B98+B03}$ denote the MFs for the joint B98 and B03 map. This expression is used to derive constraints for $f_{\rm NL}$ and for our goodness-of-fit analysis. The full covariance matrix $C_{J,J'}$ is also estimated from Gaussian Monte Carlo simulations. We have verified that, when computing its matrix elements, one needs to take into account the correlations among different functionals not to incur in biased constraints. In Fig. 2 we plot each MF of the B98 and B03 data compared with the theoretical predictions with the best-fitting value of $f_{\rm NL}$ for each MF. The error bars are derived as 1σ deviations estimated from 1000 Gaussian maps with correlated noise.

We study the effect that neglecting the contribution of a range of multipoles ℓ has on this analysis. A low-ℓ cut is necessary since we are dealing with data from a suborbital experiment, which has not been designed to measure large angular scales. These cannot be constrained properly, first because of the limited angular extension of the region surveyed, and secondly because timeline filtering is applied to the data to suppress contribution from low-frequency noise and systematics. The filters are applied during the map-making stage at ∼70 mHz both for B03 and B98 (Crill et al. 2003; Masi et al. 2006). While we apply the same filters in our simulations, the amount of low-ℓ power in the latter is somewhat different from

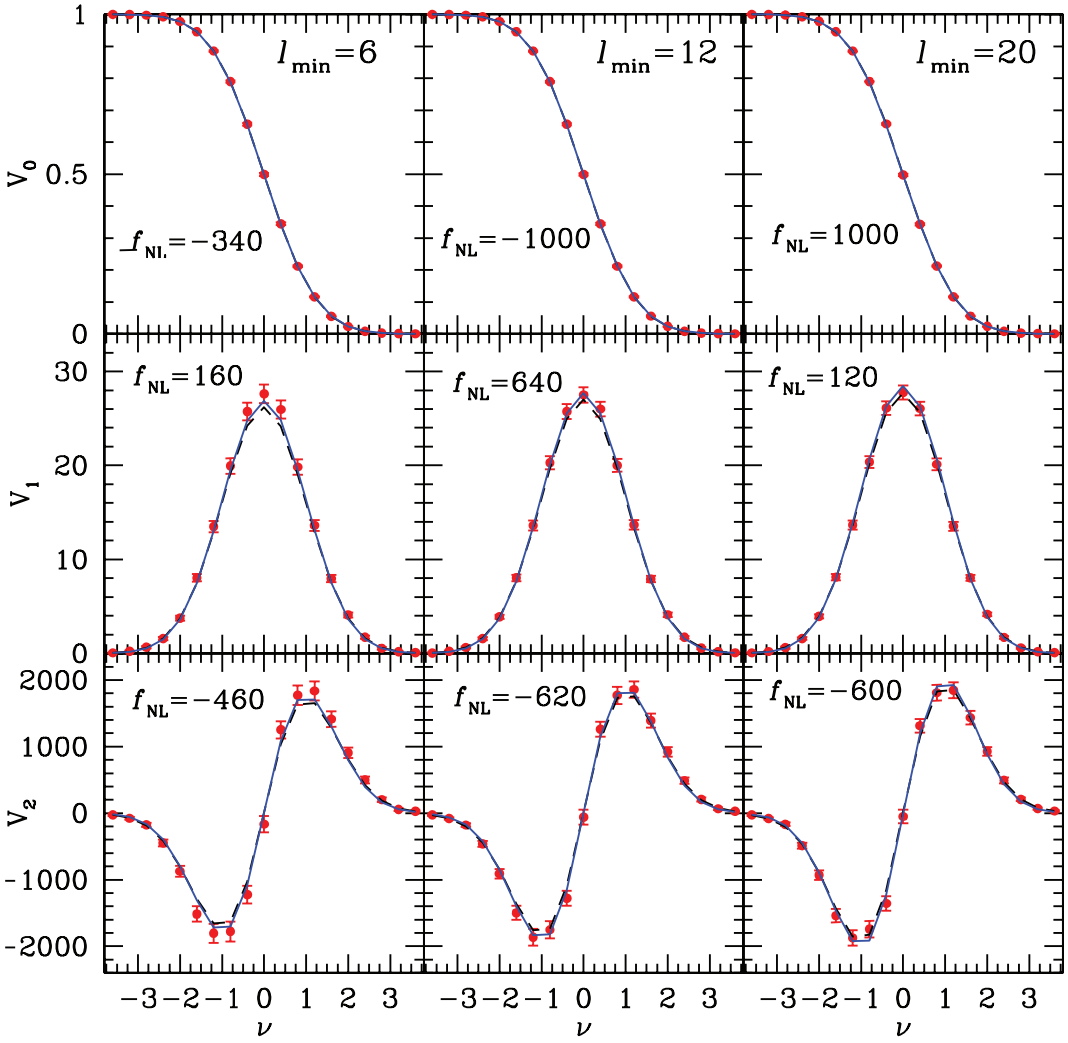

Figure 2. The plots show, from top to bottom, V_0, V_1 and V_2 computed from the BOOMERanG data (filled circles), from analytical formulae (solid line, here computed with the best-fitting f_{NL} value for each functional) and from Gaussian Monte Carlo simulations (dashed lines). The columns refer to different choices of the low-ℓ cut (see text), $\ell_{min} = 6$, 12 and 20 (from left- to right-hand side). The error bars for the data are derived as the 1σ standard deviation of our Monte Carlo simulations. The pixel size of the map is ∼7 arcmin (HEALPIX $N_{side} = 512$).

those exhibited by the data. This happens because the GLS map maker is more efficient in recovering the large-scale structure from the simulations, where we only add Gaussian noise with random phases, rather than from the data where the noise has a more complex structure. To account for this effect, we exploit one degree of freedom allowed by the harmonic analysis to MF pursued here: specifically, we set to zero all the power in the map below ℓ_{min}. The left- to right-hand panels of Fig. 2 refer to three different choices: $\ell_{min} = 6$, 12 and 20, respectively. The $\ell_{min} = 6$ cut is the natural one that would arise due to limited sky coverage but in this case the MFs from data and simulations do not agree well for V_1 and V_2 (see Fig. 2). The agreement is much better for $\ell_{min} = 12$ and 20 with no appreciable difference between the two. This comes as little surprise, since a telescope scan speed in the range 0.5–1 dps (both speeds have been employed in the data set we consider) effectively high-pass filters the data in the range $10 \lesssim \ell \lesssim 20$. (Note, however, that timeline filtering has an anisotropic effect on the sky, due to the nature of the scanning strategy employed for BOOMERanG.)

On the other hand, it is advantageous to consider also a high-ℓ cut ℓ_{max} to probe how the decreasing S/N level can affect f_{NL} constraints. For the data, this can be done by varying the HEALPIX resolution parameter N_{side} which is linked to ℓ_{max} in the spherical harmonic transform. We first focus in the following on $N_{side} = 256$ with $\ell_{max} = 512$ and $N_{side} = 512$ with $\ell_{max} = 1000$; we will then also consider $N_{side} = 128$ with $\ell_{max} = 256$. Our data set is signal dominated at $\ell \simeq 500$ while begins to be noise dominated at $\ell \simeq 1000$ (Jones et al. 2006).

In Fig. 3 we show the analytical non-Gaussian corrections ΔV_J (equation 12) for each MF compared to the residuals obtained by subtracting from the B98/B03 data MFs their Monte Carlo average, that is $V_J^{B98+B03} - \bar{V}_J(f_{NL} = 0)$. The error bars represent the 1σ error estimated from 1000 Gaussian Monte Carlo simulations. The analytical residuals are computed using the best-fitting value of f_{NL} as obtained by minimizing the χ^2 in equation (14), albeit this is done separately for each MF, ignoring (only for the sake of this plot) correlations among different functionals. The analytical ΔV_J in Fig. 3 are normalized to the maximum of their Gaussian part, while the data points are normalized to the maximum of the Monte Carlo average. We show results both for $N_{side} = 256$ (left-hand side) and for $N_{side} = 512$ (right-hand side) and for a low multiple cut at

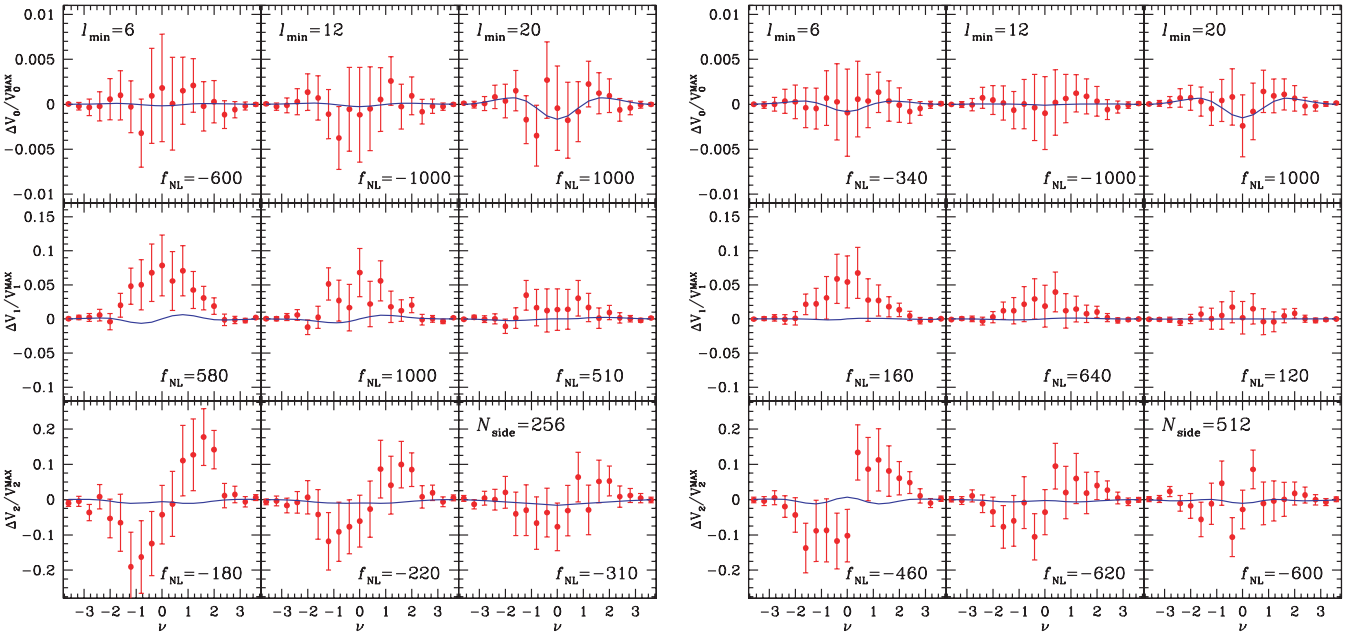

Figure 3. Comparison of the three MF residuals for B98/B03 temperature data (filled circles) to the analytical predictions with the best-fitting value of f_{NL} for each functional (solid lines). The analytical predictions are normalized to the maximum value of the Gaussian part while the data points are normalized to the maximum of the Monte Carlo average. The left-hand figure is for HEALPIX $N_{side} = 256$ resolution while the right-hand figure is for $N_{side} = 512$. From left- to right-hand side in each figure, we show the $\ell_{min} = 6$, 12 and 20 cases. The error bars represent the standard deviation at 1σ estimated from 1000 Gaussian Monte Carlo simulations.

$\ell_{min} = 6$, 12 and 20 (left- to right-hand side). The agreement of the residual plots suggests that it is safer to adopt the most conservative cut at $\ell_{min} = 20$. This impression is supported by goodness-of-fit analysis. To this purpose, we compute the χ^2 value in equation (14) at best-fitting f_{NL} (for $N_{side} = 512$), limiting ourselves to V_1 and V_2 that, as the residual plots in Fig. 3 show, are most sensitive to the choice of ℓ_{min}. We find $\chi^2 = 30$, 24 and 39 for $\ell_{min} = 6$, 12 and 20, respectively, out of 38 degrees of freedom. In this goodness-of-fit analysis it is essential to take into account the full covariance matrix $C^{-1}_{J,J'}$ because the estimated values of the MF are significantly coupled. Increasing ℓ_{min} further does not yield further advantage, so we focus on $\ell_{min} = 20$ for our final analysis. It is worth emphasizing that we apply the harmonic cut to both the data and the simulations.

Table 1 lists the confidence intervals for f_{NL} estimated from the BOOMERanG data at different ℓ_{min} and ℓ_{max} thresholds. The results are obtained taking into account the full covariance matrix of the V_k values, as expressed in equation (14). The MFs computed at different HEALPIX resolution encode different statistical information on the underlying field and thereby combining two sets of MFs improve the limits on f_{NL}. We build a global covariance matrix to take also into account correlations among the two sets. We repeat this multiresolution analysis for each ℓ_{min} value considered in Table 1.

Table 2 shows in more detail the confidence intervals obtained using the multiresolution estimator. Here we focus on $\ell_{min} = 20$ and include also results for $N_{side} = 128$ or $\ell_{max} = 256$. At this resolution the signal is markedly suppressed by the coarse pixel window. However, strong noise suppression makes its use still beneficial in a combined multiresolution analysis.

In the conservative case of $\ell_{min} = 20$ using the 'combined' estimator for $N_{side} = 128$, 256 and 512, our χ^2 analysis yields $-450 < f_{NL} < 190$ at 1σ level and $-770 < f_{NL} < 500$ at 95 per cent CL, while the minimum (best-fitting) value of f_{NL} is at -130.

The previous analysis performed only on the B03 data set (De Troia et al. 2007) produced limits weaker than those obtained in this paper by a factor of $\simeq$1.45. One might wonder whether such an improvement derives mainly from the inclusion of the B98 data

Table 1. The confidence intervals for f_{NL} estimated for the B03/B98 data with different low- and high-ℓ cut values (see text). We show both the 1σ and 2σ confidence interval. The last two columns are obtained from a combined analysis of data for the two ℓ_{max} values. The last row is derived using a simulation with no effective low-ℓ cut and shows the improvement that could be obtained if a low-resolution pattern had been present in the BOOMERanG field.

ℓ_{min}	$\ell_{max} = 512$		$\ell_{max} = 1000$		Combined	
	1σ	2σ	1σ	2σ	1σ	2σ
6	340	660	790	1570	320	620
12	360	710	970	1930	350	690
20	380	730	910	1830	350	710
2	260	510	470	920	260	510

Table 2. Summary of 1σ and 2σ confidence intervals for f_{NL} obtained at $\ell_{min} = 20$ for several resolutions (or effective ℓ_{max}) and their multiresolution combination (see text). The joint B98 + B03 data set is considered.

N_{side}	1σ	2σ
128 ($\ell_{max} = 256$)	550	1100
256 ($\ell_{max} = 512$)	380	730
512 ($\ell_{max} = 1000$)	910	1830
128 + 256	330	650
128 + 512	480	950
256 + 512	350	710
128 + 256 + 512	320	640

Table 3. Confidence intervals for $f_{\rm NL}$ estimated separately for B98 and B03, derived $\ell_{\rm min} = 20$ and two $\ell_{\rm max}$ choices, as well as for their combined multiresolution analysis (see text). Both 1σ and 2σ intervals are given.

Data set	$\ell_{\rm max} = 512$		$\ell_{\rm max} = 1000$		Combined	
	1σ	2σ	1σ	2σ	1σ	2σ
B98	480	950	1830	3640	460	910
B03	380	760	830	1650	360	730

set or from the new analysis method employed in this paper. To answer this question, we have analysed the B98 and B03 data sets separately. We find that both B98 and B03 are separately consistent with a null $f_{\rm NL}$ hypothesis, with the confidence intervals shown in Table 3. These results show how the $f_{\rm NL}$ results are completely dominated by the B03 data set. Since the latter is basically the same as that used in De Troia et al. (2007), we conclude that the improvement arises due to the new method of analysis employed. This might sound surprising at first glance: B98 has surveyed a larger sky area, which should help in reducing cosmic variance. However, it did so at the price of a worse S/N with respect to B03. Apparently, achieving excellent S/N is more important for the kind of $f_{\rm NL}$ analysis employed here than enlarging the sky fraction by almost 50 per cent. This conclusion is supported by the poor performance of the $\ell_{\rm max} = 1000$ results. In fact, the improvement with respect to the De Troia et al. (2007) analysis can be mostly ascribed to the 'combined' (multiresolution) approach employed in this paper: the previous analysis was limited to $N_{\rm side} = 512$. Working with the present method *only* at the latter resolution, and assuming $\ell_{\rm min} = 2$ in agreement with what was done in De Troia et al. (2007), we find that the resulting $f_{\rm NL}$ constraints are consistent.

We can also quantify the cost of imposing a low-ℓ cut to the data. In fact, had we not considered an effective $\ell_{\rm min}$ value, one would expect to reduce the confidence interval on $f_{\rm NL}$ by $\simeq 1.6$ (cf. the last row in Table 1, obviously obtained not from the data but from a simulation containing a low-resolution pattern). In practice, this could be obtained by adding to the data set a low-resolution CMB field coming e.g. from the *WMAP* data. While this would give us tighter constraints on $f_{\rm NL}$, we prefer to focus here on the limits one can derive from the BOOMERanG data alone. Note also that a diminished sensitivity to low-resolution features is a characteristic common to most – if not all – of the suborbital experiments. The accurate measurement of the CMB at low and high multipoles with one single experiment is rather a prerogative of space-borne missions, which enjoy the necessary stability and long-term integration capability. Our analysis is the first (to our knowledge) to explicitly take into account this effect for a suborbital experiment. To explain the significant broadening of $f_{\rm NL}$ constraints caused by the low-ℓ cut, one can note that for the underlying ('local') form of non-Gaussianity we are probing here, the low multipoles are actually very important. In fact, most of the signal in the reduced bispectrum $b_{\ell_1\ell_2\ell_3}$ lies in 'squeezed' ℓ-space triangles, with one side much smaller than the other two. When probing non-Gaussianity one is basically comparing signal at the lowest multipole with two of the highest multipoles. As a result, S/N increases as $\ell_{\rm max}/\ell_{\rm min}$ so one can either increase $\ell_{\rm max}$ for a given $\ell_{\rm min}$ (which explains, e.g. the improvement of *WMAP* over *COBE* and the forecasted improvement of *Planck* over *WMAP*) or reduce $\ell_{\rm min}$ for a given $\ell_{\rm max}$.

We finally discuss the robustness of our analysis to the significant sky cut involved here. Hikage et al. (2008) have shown that the harmonic MF approach can be safely applied over the cut sky assumed for the standard *WMAP* analysis. However, the mask used here for BOOMERanG is more restrictive. Hence, we have employed a set of non-Gaussian simulations to convince ourselves that the analytical MF predictions are in agreement with simulated results even in the case of BOOMERanG. It turns out that the low-ℓ cut $\ell_{\rm min} = 20$ is beneficial to the agreement, as one would naively expect because only the lowest multipoles are severely affected by the mask. Since the analytical and simulated MF are consistent, the $f_{\rm NL}$ results need to be in agreement as well.

5 CONCLUSIONS

We have analysed data from the BOOMERanG experiment, combining for the first time the temperature maps of the 1998 and 2003 campaigns, to constrain a non-Gaussian primordial component in the observed CMB field. We focused on MFs, comparing the data to analytical perturbative corrections in order to get constraints on the non-linear coupling parameter $f_{\rm NL}$. We have used a set of highly realistic simulation maps of the observed field generated assuming a Gaussian CMB sky, since the formalism we have adopted does not require non-Gaussian simulation maps. We studied the effect that the lack of low-resolution CMB features in the BOOMERanG data has on $f_{\rm NL}$ constraints. We find $-450 < f_{\rm NL} < 190$ at 68 per cent CL and $-770 < f_{\rm NL} < 500$ at 95 per cent CL. These limits are significantly better than those published in a previous analysis limited to the BOOOMERanG 2003 data ($-800 < f_{\rm NL} < 1050$ at 95 per cent CL), and represent the best results to date for suborbital experiments and probe angular scales smaller than those accessible to the *WMAP*.

ACKNOWLEDGMENTS

The BOOMERanG team gratefully acknowledges support from the CIAR, CSA and NSERC in Canada; Agenzia Spaziale Italiana, University La Sapienza and Programma Nazionale Ricerche in Antartide in Italy; PPARC and the Leverhulme Trust in the UK and NASA (awards NAG5-9251 and NAG5-12723) and NSF (awards OPP-9980654 and OPP-0407592) in the USA. Additional support for detector development was provided by CIT and JPL. Field, logistical and flight support were supplied by USAP and NSBF. This research used resources at NERSC, supported by the DOE under Contract No. DE-AC03-76SF00098, and CASPUR (Rome, Italy; special thanks are due to M. Botti and F. Massaioli). We also acknowledge partial support from ASI Contract I/016/07/0 'COFIS' and ASI Contract *Planck* LFI activity of Phase E2. Some of the results in this paper have been derived using the HEALPIX package (Górski et al. 2005). CH acknowledges support from the Particle Physics and Astronomy Research Council grant number PP/C501692/1 and a JSPS (Japan Society for the Promotion of Science) fellowship. We thank an anonymous referee for useful suggestions.

REFERENCES

Bartolo N., Komatsu E., Matarrese S., Riotto A., 2004, Phys. Rep., 402, 103
Bernardeau F., Uzan J.-F., 2002, Phys. Rev. D, 66, 103506
Creminelli P., Senatore L., Zaldarriaga M., Tegmark M., 2007, J. Cosmol. Astropart. Phys., 3, 5
Crill B. P. et al., 2003, ApJS, 148, 527
Cruz M., Cayón L., Martínez-González E., Vielva P., Jin J., 2007, ApJ, 655, 11
Curto A., Macías-Pérez J. F., Martínez-González E., Barreiro R. B., Santos D., Hansen F. K., Liguori M., Matarrese S., 2008, A&A, 486, 383

Curto A., Martínez-González E., Barreiro R. B., 2009, ApJ, 706, 399
de Bernardis P. et al., 2000, Nat, 404, 955
de Gasperis G., Balbi A., Cabella P., Natoli P., Vittorio N., 2005, A&A, 436, 1159
De Troia G. et al., 2003, MNRAS, 343, 284
De Troia G. et al., 2007, ApJ, 670, L73
Eriksen H. K., Banday A. J., Górski K. M., Hansen F. K., Lilje P. B., 2007, ApJ, 660, L81
Gangui A., Lucchin F., Matarrese S., Mollerach S., 1994, ApJ, 430, 447
Górski K. M., Hivon E., Banday A. J., Wandelt B. D., Hansen F. K., Reinecke M., Bartelmann M., 2005, ApJ, 622, 759
Hikage C., Komatsu E., Matsubara T., 2006, ApJ, 653, 11
Hikage C., Matsubara T., Coles P., Liguori M., Hansen F. K., Matarrese S., 2008, MNRAS, 389, 1439
Hinshaw G. et al., 2003, ApJS, 148, 135
Jones W. C. et. al., 2006, ApJ, 647, 823
Jones W. C., Bhatia R. S., Bock J. J., Lange A. E., 2003, Proc. SPIE, 4855, 227
Komatsu E., Spergel D. N., 2001, Phys. Rev. D, 63, 063002
Komatsu E. et al., 2009, ApJS, 180, 330
Komatsu E. et al., 2010, preprint (arXiv:1001.4538)
Lyth D. H., Ungarelli C., Wands D., 2003, Phys. Rev. D, 67, 23503
MacTavish C. J. et al., 2006, ApJ, 647, 799
Masi S. et al., 2006, A&A, 458, 687
Matsubara T., 2003, ApJ, 584, 1
Montroy T. E. et al., 2006, ApJ, 647, 813
Natoli P., de Gasperis G., Gheller C., Vittorio N., 2001, A&A, 372, 346
Page L. et al., 2003, ApJS, 148, 39
Park C.-G., Park C., Gott J. R., III, 2007, ApJ, 660, 959
Piacentini F. et al., 2006, ApJ, 647, 833
Pietrobon D., Cabella P., Balbi A., de Gasperis G., Vittorio N., 2009, MNRAS, 396, 1682
Polenta G. et al., 2002, ApJ, 572, L27
Räth C., Morfill G. E., Rossmanith G., Banday A. J., Górski K. M., 2009, Phys. Rev. Lett., 102, 131301
Rudjord O., Hansen F. K., Lan X., Liguori M., Marinucci D., Matarrese S., 2010, ApJ, 708, 1321
Ruhl J. E. et al., 2003, ApJ, 599, 786
Salopek D. S., Bond J. R., 1990, Phys. Rev. D, 42, 3936
Santos M. G. et al., 2003, MNRAS, 341, 623
Smith S. et al., 2004, MNRAS, 352, 887
Smith K. M., Senatore L., Zaldarriaga M., 2009, J. Cosmol. Astropart. Phys., 09, 006
Spergel D. et al., 2003, ApJS, 148, 175
Verde L., Wang L., Heavens A. F., Kamionkowski M., 2000, MNRAS, 313, 141
Vielva P., Martínez-González E., Barreiro R. B., Sanz J. L., Cayón L., 2004, ApJ, 609, 22
Yadav A. P. S., Wandelt B. D., 2008, Phys. Rev. Lett., 100, 181301

This paper has been typeset from a TEX/LATEX file prepared by the author.